



The onset of vortex instability in laminar natural convection flow over an inclined plate embedded in a porous medium

D.H. Lee^a, D.Y. Yoon^b, C.K. Choi^{a,*}

^a*School of Chemical Engineering, Seoul National University, Seoul 151-742, South Korea*

^b*Department of Chemical Engineering, Kwangwoon University, Seoul 139-701, South Korea*

Received 23 April 1999; received in revised form 15 October 1999

Abstract

The onset of vortex instability in primary laminar natural convection flow over an inclined plate embedded in a porous medium was analyzed. Forchheimer's model involving thermal dispersion was used to examine inertia effects on the onset of vortex instability. By employing the propagation theory we have developed, the critical streamwise position to mark the onset of stationary longitudinal vortex rolls was predicted. The predicted stability criteria were compared well in the range of $25^\circ \leq \gamma \leq 60^\circ$ with experiments of ionic mass transfer in aqueous CuSO_4 solution systems. Also, new mass transfer correlations of Sh_L were suggested for $0^\circ \leq \gamma \leq 60^\circ$ and $Ra_L \leq 7000$. © 2000 Elsevier Science Ltd. All rights reserved.

1. Introduction

It is well-known that a fluid layer becomes unstable when buoyancy forces accompanied by heat or mass transfer overcome dissipative forces of diffusion and viscosity. The convective motion driven by buoyancy forces in an initially quiescent fluid layer has been analyzed extensively since Benard's [1] systematic experiments and Lord Rayleigh's [2] theoretical analysis were reported. Similar to this convective motion, secondary motion in the form of longitudinal vortex rolls can set in due to buoyancy forces in primary natural convection over inclined surfaces heated from below. The related experimental evidence was reported first by

Sparrow and Husar [3]. Subsequent experimental investigations by Lloyd and Sparrow [4] clearly showed that for inclined angles in excess of 17° relative to the vertical, the instability is characterized by longitudinal vortices. These experimental observations have prompted a number of theoretical studies on the onset of longitudinal vortex rolls in natural convection flow over inclined surfaces. Linear stability analyses were performed by Hwang and Cheng [5], Haaland and Sparrow [6], Chen and Tzuoo [7] and Hwang et al. [8] for pure fluid layers. This roll-type instability is encountered in various processing systems such as heat exchangers, electroplating and chemical vapor deposition. Most of these processes involve non-linear, developing temperature or concentration profiles and therefore it becomes an important problem to predict when or where the instability sets in.

The buoyancy-induced motion in a fluid layer through a permeable material is also an important

* Corresponding author. Tel.: +82-2-880-7407; fax: +82-2-888-7295.

E-mail address: ckchoi@plaza.snu.ac.kr (C.K. Choi).

Nomenclature

a	dimensional spanwise wave number	u, v, w	velocities in x -, y - and z -direction
A	coefficient in Eq. (49)	x, y, z	axial, spanwise and normal coordinate
\tilde{a}	dimensionless wave number	<i>Greek symbols</i>	
a^*	dimensionless wave number based on length scaling factor $\tilde{x}^{1/2}$, $\tilde{a}\tilde{x}^{1/2}$	α_0	effective molecular thermal diffusivity
b	Forchheimer constant	α_T	effective thermal dispersion coefficient
B	transverse thermal dispersion constant	δ_T	dimensionless thermal boundary-layer thickness, $\Delta_T \overline{Ra}_L^{1/2} / (\zeta_T L)$
D_0	effective molecular mass diffusivity	Δ_T	dimensional thermal boundary-layer thickness, $\zeta_T x / \overline{Ra}_x^{1/2}$
d_p	particle diameter	ε	porosity
f	dimensionless base-state stream function	γ	inclination angle with respect to vertical
g	gravitational acceleration constant	θ	dimensionless temperature
Gr	Grashof number, $g\beta b K^2 \Delta T / \nu^2$ or $g b K^2 \Delta \rho / (\nu^2 \rho_b)$	ψ	base-state stream function
h_x	local heat or mass transfer coefficient	ζ	similarity variable, $(Ra_x \cos \gamma)^{1/2} z/x$ or $\overline{Ra}_x^{1/2} z/x$
h_L	average h -value over plate length L	ζ_T	ζ -value where θ_0 has a value 0.01
K	permeability	<i>Subscripts</i>	
k_0	effective molecular thermal conductivity	b	bulk state
L	plate length	c	critical values
Nu_x	local Nusselt number, $h_x x / k_0$	0	basic undisturbed quantities
Ra_d	Darcy–Rayleigh number based on d_p	1	disturbed quantities
Ra_L	Darcy–Rayleigh number, $g\beta K \Delta T L / (\alpha_0 \nu)$ or $g K L \Delta \rho / (D_0 \nu \rho_b)$	<i>Overbars</i>	
Ra_x	local Darcy–Rayleigh number based on x	–	modified parameters involving $\cos \gamma$
Re_p	Reynolds number having the length scale d_p , $u_{avg} d_p / \nu$	~	dimensionless velocity or coordinates
Sh_L	average Sherwood number, $h_L L / D_0$		
t	time		

mechanism of transport. Cheng and Minkowycz [9] presented a similarity analysis for a vertical flat plate embedded in a fluid-saturated porous medium. For an inclined surface Hsu and Cheng [10] showed that, in the basic laminar-flow analysis, the boundary layer flow over an inclined heated plate can be approximated by the similarity solutions for a vertical plate and then the vortex instability was analyzed. Jang and Chang [11] re-examined the analyses. All of these investigations are based on the Darcy flow. However at high flow rates or in porous media of high permeability, there is a departure from Darcy's law and the inertia effects become significant. To study laminar natural convection from a vertical plate embedded in a porous medium the Forchheimer equation was used first by Plumb and Huenefeld [12]. The inertia effects on the vortex mode of instability of secondary natural convection flow in a porous medium were examined first by Chang and Jang [13]. They showed that the inertia effects make the system more unstable in a horizontal system. But their interpretation on the Forchheimer equation is found to be incorrect,

which will be discussed later. Therefore it may be stated that the stability analysis, using the Forchheimer equation properly, on the vortex mode of instability of buoyancy-induced boundary layer flow in a porous medium has not been investigated. In the case when inertia effects are prevalent, the transverse thermal dispersion effect is expected to become important. Plumb [14] studied this dispersion effect on buoyancy-induced boundary layers from a vertical plate embedded in a porous medium. Hong et al. [15] examined analytically the no-slip effect and the inhomogeneity in permeability and porosity as well as the inertia and dispersion effects for the same system. Based on these studies, the stability criteria of buoyancy-induced boundary-layer flow over an inclined plate embedded in a porous medium will be examined by considering both inertia and dispersion effects.

The foregoing problems in heat transfer can be applied to the similar mass transfer systems. To complement the reported predictions, experimental results of copper electroplating in aqueous copper sulfate solution are also reported.

2. Stability analysis

2.1. Basic-state flow and temperature fields

The system considered here is a fluid-saturated porous medium as is shown in Fig. 1. A Cartesian frame of reference is chosen where the x -axis is aligned with a flat plate with an inclination angle γ with respect to the vertical, the y -axis is in the spanwise direction and the z -axis is perpendicular to the plate. The ambient temperature of the porous medium is uniform at T_∞ and the wall temperature is kept at a higher value T_w . Under this condition primary steady laminar natural convection prevails and its velocity fields consist of u_0 and w_0 . In this figure Δ_T denotes the thermal boundary-layer thickness. The following conventional assumptions simplify the analysis [10–14]: the fluid and the porous medium are in local thermal equilibrium, the porous medium is everywhere isotropic and homogeneous, the Boussinesq approximation is valid and Forchheimer’s model is used for the momentum equations. Now, the following dimensionless variables are introduced:

$$\zeta = \frac{z}{x}(Ra_x \cos \gamma)^{1/2} \tag{1}$$

$$\psi = \alpha_0(Ra_x \cos \gamma)^{1/2}f(\zeta) \tag{2}$$

$$\theta_0(\zeta) = \frac{T_0 - T_\infty}{T_w - T_\infty} \tag{3}$$

where Ra_x is the Darcy–Rayleigh number defined as

$$Ra_x = \frac{g\beta K(T_w - T_\infty)x}{\alpha_0\nu} \tag{4}$$

ζ denotes the similarity variable based on the thermal boundary-layer thickness Δ_T having the order of mag-

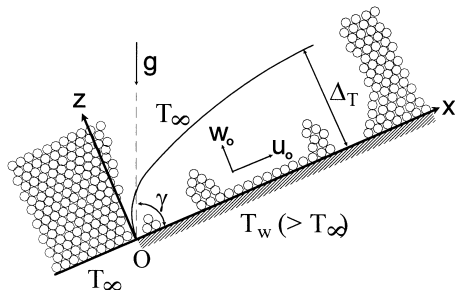


Fig. 1. Schematic diagram of the heat transfer system considered here.

nitude $x(Ra_x \cos \gamma)^{-1/2}$, ψ the stream function, $f(\zeta)$ the dimensionless stream function, $\theta_0(\zeta)$ the dimensionless temperature, g the gravitational acceleration constant, β the thermal expansion coefficient, ν the kinematic viscosity of fluid, and α_0 the effective molecular thermal diffusivity. The permeability K is expressed in terms of the particle diameter d_p and the porosity ε as

$$K = \frac{\varepsilon^3}{150(1 - \varepsilon)^2}d_p^2 \tag{5}$$

With the above definitions, the dimensionless basic state temperature and velocity profiles for $0^\circ \leq \gamma \leq 60^\circ$ can be represented, based on the work of Hsu and Cheng [10] and Plumb [14], as

$$(1 + \overline{Gr}f')f' - \theta_0 = 0 \tag{6}$$

$$(1 + \bar{B}Ra_d f')\theta_0'' + \left(\frac{1}{2}f + \bar{B}Ra_d f''\right)\theta_0' = 0 \tag{7}$$

subject to the boundary conditions:

$$f(0) = 0, \quad \theta_0(0) = 1, \quad f'(\infty) = 0, \quad \theta_0(\infty) = 0 \tag{8}$$

where $\bar{B} = B \cos \gamma$ and $Ra_d = g\beta K(T_w - T_\infty)d_p/\alpha_0\nu$. B is a dispersion constant. Plumb [14] assumed that the thermal dispersion coefficient α_T due to transverse thermal dispersion would be proportional to the dominant velocity components, i.e., $\alpha_T = Bd_p u_0$. This is symbolized by $\bar{B}Ra_d f''$ in Eq. (7). The primes on the basic undisturbed quantities indicate derivatives with respect to ζ . \overline{Gr} is a modified Grashof number defined as

$$\overline{Gr} = Gr \cos \gamma = \frac{g\beta b K^2(T_w - T_\infty)}{\nu^2} \cos \gamma \tag{9}$$

which represents the relative importance of inertia effects, based on the streamwise component of gravity. The Forchheimer constant b is given by

$$b = \frac{1.75(1 - \varepsilon)}{\varepsilon^3 d_p} \tag{10}$$

As $b \rightarrow 0$ and $B \rightarrow 0$, Eqs. (6)–(8) reduce to Darcian case. This limiting one was analyzed by Hsu and Cheng [10]. The similarity solutions given by Eqs. (6)–(8) are obtained based on the boundary layer approximation but they are not valid for $\gamma > 60^\circ$. From Eqs. (2), (6) and (7) the velocity components and the local Nusselt number for the basic undisturbed flow are given as

$$u_0 = \frac{\alpha_0}{x}(Ra_x \cos \gamma)f' \tag{11}$$

$$w_0 = \frac{\alpha_0}{2x} (Ra_x \cos \gamma)^{1/2} (\xi f' - f) \quad (12)$$

$$Nu_x = -[1 + \bar{B} Ra_d f'(0)] \theta'_0(0) (Ra_x \cos \gamma)^{1/2}. \quad (13)$$

2.2. Disturbance equations

By following the well-known linear stability analysis, the variables in the flow and temperature fields are decomposed into the basic undisturbed quantities and their infinitesimal disturbances as

$$T(x, y, z, t) = T_0(x, z) + T_1(x, y, z, t)$$

$$p(x, y, z, t) = p_0(x, z) + p_1(x, y, z, t)$$

$$u(x, y, z, t) = u_0(x, z) + u_1(x, y, z, t)$$

$$v(x, y, z, t) = v_1(x, y, z, t)$$

$$w(x, y, z, t) = w_0(x, z) + w_1(x, y, z, t) \quad (14)$$

where the three-dimensional (3D) disturbances are denoted by the subscript '1' and the two-dimensional (2D) basic undisturbed quantities by the subscript '0'. t represents time.

The disturbances are assumed to be periodic horizontally under the normal mode analysis. For example, the vertical velocity disturbance w_1 can be described as

$$w_1(x, y, z, t) = w_1^*(x, y, z) \exp[i(a_x x + a_y y) + \sigma t] \quad (15)$$

where i denotes the imaginary number, a_x the streamwise periodic wave number, a_y the spanwise periodic one, and σ the temporal growth rate. It is worth noting that a_x , a_y and σ are all real for regular vortex disturbances and $\sigma = 0$ for neutral stability. With $\sigma = 0$ the disturbances are assumed to be functions of space variables alone. Now, after substituting Eq. (14) into the governing equations for the 3D convective flow in a porous medium, the following linearized disturbance equations are obtained:

$$\frac{\partial u_1}{\partial x} + \frac{\partial v_1}{\partial y} + \frac{\partial w_1}{\partial z} = 0 \quad (16)$$

$$\left(\frac{v}{K} + b|\mathbf{u}_0|\right) u_1 = -\frac{1}{\rho_\infty} \frac{\partial p_1}{\partial x} + g\beta \cos \gamma T_1 \quad (17)$$

$$\left(\frac{v}{K} + b|\mathbf{u}_0|\right) v_1 = -\frac{1}{\rho_\infty} \frac{\partial p_1}{\partial y} \quad (18)$$

$$\left(\frac{v}{K} + b|\mathbf{u}_0|\right) w_1 = -\frac{1}{\rho_\infty} \frac{\partial p_1}{\partial z} + g\beta \sin \gamma T_1 \quad (19)$$

$$\begin{aligned} u_0 \frac{\partial T_1}{\partial x} + u_1 \frac{\partial T_0}{\partial x} + w_0 \frac{\partial T_1}{\partial z} + w_1 \frac{\partial T_0}{\partial z} \\ = \alpha_0 \left(\frac{\partial^2 T_1}{\partial x^2} + \frac{\partial^2 T_1}{\partial y^2} + \frac{\partial^2 T_1}{\partial z^2} \right) + Bd_p \frac{\partial}{\partial z} \left(u_0 \frac{\partial T_1}{\partial z} \right. \\ \left. + u_1 \frac{\partial T_0}{\partial z} \right) \end{aligned} \quad (20)$$

where ρ_∞ denotes bulk fluid density and $|\mathbf{u}_0| = lb = \sqrt{u_0^2 + w_0^2}$. The term $Bd_p u$ represents the thermal dispersion. Hsu and Cheng [10] neglected the terms $\partial u_1/\partial x$, $\partial p_1/\partial x$ and $\partial^2 T_1/\partial x^2$ in Eqs. (16), (17) and (20) and most of the early studies on this kind of stability problems have employed this assumption. But in the present study the term $\partial u_1/\partial x$ is retained.

2.3. Propagation theory

The propagation theory employed to find the critical streamwise position ' x_c ' to mark the onset of longitudinal vortex is based on the assumption that disturbances are propagated mainly within the thermal boundary-layer thickness Δ_T at $x_c \gg \Delta_T$. In this case it is assumed that the following scale analysis at $x \cong x_c$ would be valid for disturbed quantities of Eqs. (19) and (20), respectively:

$$\frac{v}{K} w_1 \sim g\beta \sin \gamma T_1 \quad (21)$$

$$w_1 \frac{\partial T_0}{\partial z} \sim \alpha_0 \frac{T_1}{\Delta_T^2}. \quad (22)$$

From relations (21) and (22) the following peculiar relations are obtained:

$$w_1 \sim \frac{g\beta K \sin \gamma}{v} T_1 \quad (23)$$

$$\begin{aligned} \frac{\partial T_0}{\partial z} \sim \frac{\alpha_0 v}{g\beta K \sin \gamma \Delta_T^2} = \frac{\Delta T}{\Delta_T} \left(\frac{g\beta K \Delta T \Delta_T \sin \gamma}{\alpha_0 v} \right)^{-1} \\ = \frac{\Delta T}{\Delta_T} (\bar{Ra}_{\Delta_T} \tan \gamma)^{-1} \end{aligned} \quad (24)$$

where \bar{Ra}_{Δ_T} is the modified Darcy–Rayleigh number having the length scale Δ_T . \bar{Ra}_L having the length scale L is interrelated with \bar{Ra}_{Δ_T} as

$$\bar{Ra}_{\Delta_T} = \bar{Ra}_L \frac{\Delta_T}{L} \quad (25)$$

where L is the characteristic streamwise length, usually

the plate length. Now, $\overline{Ra}_{\Delta T}$ is assumed to be a constant at $x \cong x_c$ for a given γ and L . Then, the following relation is obtained:

$$\Delta T \sim \left(\frac{g\beta K \sin \gamma}{\alpha_0 v} \Delta T \right)^{-1} \tag{26}$$

which means that both the critical position x_c and the corresponding ΔT decrease with increasing ΔT since $\Delta T \Delta T \cong \text{constant}$ in Eq. (26).

From the above relations, Eqs. (21) and (22) are nondimensionalized as

$$\frac{\tilde{w}_1}{\delta_T} \sim \theta_1 \tag{27}$$

$$\overline{Ra}_L \tan^2 \gamma \tilde{w}_1 \frac{\partial \theta_0}{\partial \tilde{z}} \sim \frac{\theta_1}{\delta_T^2} \tag{28}$$

where δ_T is the dimensionless thermal boundary-layer thickness defined as $\Delta T / \Delta T_{T,L}$ and it has the order of magnitude of $(x/L)^{1/2}$. $\Delta T_{T,L}$ denotes the thermal boundary-layer thickness at $x = L$. \tilde{w}_1 denotes the dimensionless velocity disturbance in the z -direction and \tilde{z} the dimensionless vertical distance. These are defined below. The dimensionless temperature disturbance θ_1 is defined as $g\beta KL \sin \gamma \tan \gamma T_1 / (\alpha_0 v)$. δ_T in relation (27) is produced when ΔT in \overline{Ra}_L is replaced with the right-hand side term of relation (26). Relations (27) and (28) are similar to those of Hsu and Cheng [10] but the term \overline{Ra}_L appears in relation (28) because of their different nondimensionalization of disturbed quantities. Relations (27) and (28) mean that the secondary longitudinal vortex occurs due to θ_1 and the incipient secondary flow is very weak at $x = x_c$. In this viewpoint the basic state temperature and its disturbance have been nondimensionalized having different scales. Similar treatments can be found in thermal instability analyses by Hwang and Choi [16], Kang and Choi [17] and Kim et al. [18,19].

Now, on the basis of the scales of the thermal boundary-layer thickness and the basic state velocity, the following dimensionless variables are defined:

$$(\tilde{x}, \tilde{y}, \tilde{z}) = \frac{1}{L} (x, \overline{Ra}_L^{1/2} y, \overline{Ra}_L^{1/2} z) \tag{29}$$

$$(\tilde{u}_0, \tilde{w}_0) = \frac{L}{\alpha_0 \overline{Ra}_L} (u_0, \overline{Ra}_L^{1/2} w_0) \tag{30}$$

$$(\tilde{u}_1, \tilde{v}_1, \tilde{w}_1) = \frac{L}{\alpha_0 \overline{Ra}_L} (u_1, \overline{Ra}_L^{1/2} v_1, \overline{Ra}_L^{1/2} w_1) \tag{31}$$

$$\tilde{p}_1 = \frac{K}{\mu \alpha_0} p_1. \tag{32}$$

Then the disturbance equations are represented under the usual boundary-layer theory, i.e. $\partial \tilde{p}_1 / \partial \tilde{x} = \partial^2 \theta_1 / \partial \tilde{x}^2 = 0$ by the following dimensionless equations:

$$\frac{\partial \tilde{u}_1}{\partial \tilde{x}} + \frac{\partial \tilde{v}_1}{\partial \tilde{y}} + \frac{\partial \tilde{w}_1}{\partial \tilde{z}} = 0 \tag{33}$$

$$(1 + \overline{Gr} |\tilde{u}_0|) \tilde{u}_1 = \frac{\theta_1}{\overline{Ra}_L \tan^2 \gamma} \tag{34}$$

$$(1 + \overline{Gr} |\tilde{u}_0|) \tilde{v}_1 = -\frac{\partial \tilde{p}_1}{\partial \tilde{y}} \tag{35}$$

$$(1 + \overline{Gr} |\tilde{u}_0|) \tilde{w}_1 = -\frac{\partial \tilde{p}_1}{\partial \tilde{z}} + \frac{\theta_1}{\overline{Ra}_L^{1/2} \tan \gamma} \tag{36}$$

$$\begin{aligned} \tilde{u}_0 \frac{\partial \theta_1}{\partial \tilde{x}} + \tilde{w}_0 \frac{\partial \theta_1}{\partial \tilde{z}} + \overline{Ra}_L \tan^2 \gamma \left(\tilde{u}_1 \frac{\partial \theta_0}{\partial \tilde{x}} + \tilde{w}_1 \frac{\partial \theta_0}{\partial \tilde{z}} \right) \\ = \frac{\partial^2 \theta_1}{\partial \tilde{y}^2} + \frac{\partial^2 \theta_1}{\partial \tilde{z}^2} + \overline{B} Ra_d \frac{\partial}{\partial \tilde{z}} \left(\tilde{u}_0 \frac{\partial \theta_1}{\partial \tilde{z}} \right. \\ \left. + \overline{Ra}_L \tan^2 \gamma \tilde{u}_1 \frac{\partial \theta_0}{\partial \tilde{z}} \right) \end{aligned} \tag{37}$$

with the boundary conditions,

$$\tilde{u}_1 = \tilde{v}_1 = \tilde{w}_1 = \theta_1 = 0 \quad \text{for } \zeta = 0 \text{ and } \zeta \rightarrow \infty \tag{38}$$

where $\zeta = \tilde{z} / \tilde{x}^{1/2}$, $\tilde{u}_0 = f'$, $\tilde{w}_0 = (\zeta f' - f) / (2\tilde{x}^{1/2})$ and $|\tilde{u}_0| = (\tilde{u}_0^2 + \overline{Ra}_L^{-1} \tilde{w}_0^2)^{1/2}$. ζ , \tilde{u}_0 and \tilde{w}_0 are nondimensionalized forms of Eqs. (1), (11) and (12), respectively. We assume that steady disturbance quantities are periodic with the wave number a in the spanwise y -direction. This means that in Eq. (15) $w_1^* = w_1^*(x, z)$, $a_x = 0$, $a_y = a$ and $\sigma = 0$.

Since the present analysis involves the x -dependence, the incipient disturbances will experience the spatial growth. The scale analyses on \tilde{u}_1 , \tilde{v}_1 and \tilde{p}_1 are conducted like that of \tilde{w}_1 , as is illustrated through Eqs. (21)–(28). Then for the regular longitudinal vortex rolls the dimensionless disturbance quantities are expressed as

$$\begin{bmatrix} \tilde{u}_1(\tilde{x}, \tilde{y}, \tilde{z}) \\ \tilde{v}_1(\tilde{x}, \tilde{y}, \tilde{z}) \\ \tilde{w}_1(\tilde{x}, \tilde{y}, \tilde{z}) \\ \tilde{p}_1(\tilde{x}, \tilde{y}, \tilde{z}) \\ \theta_1(\tilde{x}, \tilde{y}, \tilde{z}) \end{bmatrix} = \begin{bmatrix} \tilde{x} & u^*(\zeta) \\ 1/\tilde{a} & v^*(\zeta) \\ \tilde{x}^{1/2} & w^*(\zeta) \\ \tilde{x} & p^*(\zeta) \\ & \theta^*(\zeta) \end{bmatrix} \exp(i\tilde{a}\tilde{y}) \tag{39}$$

which satisfies Eqs. (33)–(37). \tilde{a} denotes the dimensionless wave number $[= aL / \overline{Ra}_L^{1/2}]$. It is stressed that δ_T

has the order of magnitude of $\tilde{x}^{1/2}$ and the resulting continuity equation is a function of ζ alone. Since δ_T or \tilde{x} is small, the relation of $|\tilde{u}_1| < |\tilde{w}_1|$ is kept but $|\partial\tilde{u}_1/\partial\tilde{x}|$ has the same order of magnitude as $|\partial\tilde{w}_1/\partial\tilde{x}|$. Thus in the continuity equation, the term $\partial\tilde{u}_1/\partial\tilde{x}$ is retained. This is the major difference between the propagation theory and the models of Hsu and Cheng [10] and Jang and Chang [11]. The relation of $\tilde{v}_1 = v^*(\zeta)/\tilde{a}$ is a peculiar one we have suggested [16–19] and it is believed that this makes the resulting continuity equation more reasonable.

Substituting Eq. (39) into Eqs. (33)–(38) and eliminating v^* and p^* , we can obtain the new stability equations:

$$(1 + \overline{Gr}|\tilde{u}_{01}|)u^* = \frac{\theta^*}{\overline{Ra}_x \tan^2 \gamma} \quad (40)$$

$$\begin{aligned} (1 + \overline{Gr}|\tilde{u}_{01}|)(D^2 - a^{*2})w^* \\ = \frac{1}{2}(1 + \overline{Gr}|\tilde{u}_{01}|)(\zeta D^2 u^* - Du^*) + (\overline{Gr}D|\tilde{u}_{01}|) \\ \times \left(\frac{\zeta}{2} Du^* - u^* - Dw^* \right) - \frac{a^{*2} \theta^*}{\overline{Ra}_x^{1/2} \tan \gamma} \end{aligned} \quad (41)$$

$$\begin{aligned} (1 + \overline{B}Ra_d f') D^2 \theta^* - a^{*2} \theta^* \\ = - \left(\frac{1}{2} f + \overline{B}Ra_d f'' \right) D \theta^* \\ - \overline{B}Ra_d \overline{Ra}_x \tan^2 \gamma u^* D^2 \theta_0 + \overline{Ra}_x \tan^2 \gamma \left(w^* \right. \\ \left. - \frac{\zeta}{2} u^* - \overline{B}Ra_d Du^* \right) D \theta_0 \end{aligned} \quad (42)$$

with the following boundary conditions:

$$w^* = \theta^* = 0 \quad \text{for } \zeta = 0 \text{ and } \zeta \rightarrow \infty \quad (43)$$

where $D = d/d\zeta$, $|\tilde{u}_{01}|^2 = f'^2 + (\zeta f' - f)^2 (4\overline{Ra}_x)^{-1}$, $a^* = \tilde{x}^{1/2} \tilde{a}$ and $\overline{Ra}_x = \tilde{x} \overline{Ra}_L$. The above transformations are possible since $\partial(\cdot)/\partial\tilde{x} = -(1/2)(\zeta/\tilde{x})\partial(\cdot)/\partial\zeta$ and nondimensionalization of the energy equation produces the term $\overline{Ra}_L \tan^2 \gamma \tilde{u}_1 \cdot \nabla \theta_0$ shown in Eq. (37). Also, it is noted that relations (24) and (28) are reasonable since $\overline{Ra}_x \sim (\overline{Ra}_{\Delta T})^2$. The parameters a^* and \overline{Ra}_x based on the length scaling factor $\tilde{x}^{1/2}$ are assumed to be eigenvalues. Since θ_0 , f , u^* , w^* and θ^* in Eqs. (40)–(43) are functions of ζ alone, treatment like a set of similarity transformation is possible. Now, the minimum value of $\overline{Ra}_x \tan^2 \gamma$ for a given set of \overline{Gr} , $\overline{B}Ra_d$ and γ is sought. In other words, the minimum value of \tilde{x} , i.e. \tilde{x}_c , is found for a given set of $\overline{Ra}_L \tan^2 \gamma$, \overline{Gr} , $\overline{B}Ra_d$ and γ . It is stressed that the whole procedure described

above is the essence of the propagation theory we have developed. The propagation theory may be regarded as an extension of local stability analyses.

2.4. Solution method

In order to obtain the stability criteria, the basic state flow and temperature profiles must be obtained from Eqs. (6)–(8), a priori. For this purpose the shooting method was employed to solve the two-point boundary-value problem. The implicit stiff method was used for the integration of the base flow equations and the iteration was carried out until the error at the upper boundary was less than 10^{-10} by employing the Newton–Raphson method. By this procedure the lower boundary condition of the primary flow was determined.

The disturbance equations were calculated by using the procedure similar to that for the base-flow equations. Eqs. (40)–(43) were solved by employing the outward shooting scheme of Chen and Chen [20]. In order to integrate these stability equations, the known lower boundary conditions of the basic-state equations, i.e. $f'(0)$ and $\theta'_0(0)$ were read and the proper values of Dw^* and $D\theta^*$ at $\zeta = 0$ were assumed for a given \overline{Gr} , $\overline{B}Ra_d$, γ and a^* . Since the stability equations and the boundary conditions are all homogeneous, the value of Dw^* at $\zeta = 0$ can be assigned arbitrarily and the value of the parameter $\overline{Ra}_x \tan^2 \gamma$ is assumed. This procedure can be understood easily by taking into account the characteristics of eigenvalue problems. After all the values at $\zeta = 0$ are provided, this eigenvalue problem can be proceeded numerically.

Integration was performed from the heated surface $\zeta = 0$ to a fictitious outer boundary with the fourth-order Runge–Kutta–Gill method. If the guessed values of $\overline{Ra}_x \tan^2 \gamma$ and $D\theta^*(0)$ are correct, w^* and θ^* will vanish at the outer boundary. To improve the initial guesses the Newton–Raphson iteration was used and relative errors were taken as convergence criteria. When all the relative errors were less than 10^{-10} , the outer boundary was increased by a predetermined value and the above procedure was repeated. Since the disturbances decay exponentially outside the thermal boundary-layer, an incremental change in $\overline{Ra}_x \tan^2 \gamma$ also decays fast with an increase in outer boundary depth. This behavior enables us to extrapolate the eigenvalue $\overline{Ra}_x \tan^2 \gamma$ to the infinite depth. The effect of the integration depth on the critical condition was treated intensively by Chen [21], Chen et al. [22] and Kim [23]. They showed that the present extrapolation by the Shanks transformation [24] is a good approximation to treat the infinite outer boundary. The whole numerical procedure is described in the work of Chen [21] and Kim [23].

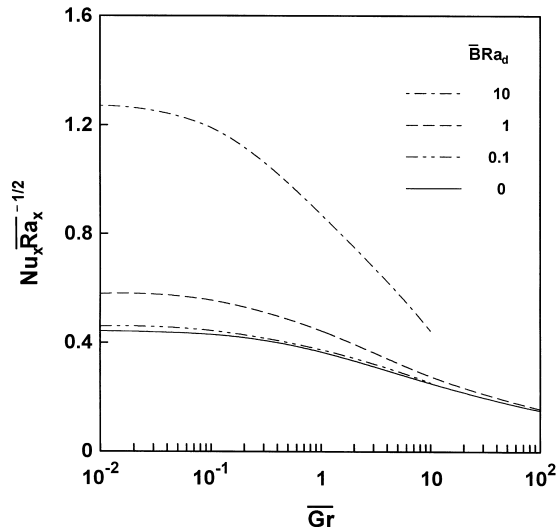


Fig. 2. Combined effects of inertia and thermal dispersion on local Nusselt number.

2.5. Results and comparison

In the present system the dimensionless basic velocity on the wall $f'(0)$ and the dimensionless temperature gradient at the wall $\theta'_0(0)$ are functions of \bar{Gr} and $\bar{B}Ra_d$. The results on Nu_x are shown in Fig. 2. $Gr = B = 0$ implies the Darcy flow. The inertia and dispersion terms show pronounced effects on the heat transfer for values of $\bar{Gr} > 0.1$ and $\bar{B}Ra_d > 1$. The inertia effect decreases Nu_x whereas the thermal dispersion increases Nu_x .

The $\bar{Ra}_x \tan^2 \gamma$ - and a^* -values obtained from the present stability equations constitute the neutral stability curves, as shown in Figs. 3 and 4. The present minimum $\bar{Ra}_x \tan^2 \gamma$, i.e. $\bar{Ra}_{x,c} \tan^2 \gamma$ for the case of $Gr = B = 0$ is compared well with those of Hsu and Cheng [10], as is seen in Table 1. The $\bar{Ra}_{x,c} \tan^2 \gamma$ -value

Table 1
Comparison of critical values for $B = 0$ and $\gamma = 40^\circ$

\bar{Gr}	$\partial u_1 / \partial x$	a_c^*	$\bar{Ra}_{x,c} \tan^2 \gamma$
0	Retained	0.662	120.0
	Neglected	0.635	120.7
	Hsu and Cheng [10]	0.636	120.7
0.1	Retained	0.643	123.2
	Neglected	0.619	123.8
1	Retained	0.563	144.9
	Neglected	0.543	144.0
10	Retained	0.399	245.7
	Neglected	0.381	237.9
100	Retained	0.24	578.6
	Neglected	0.225	538.7

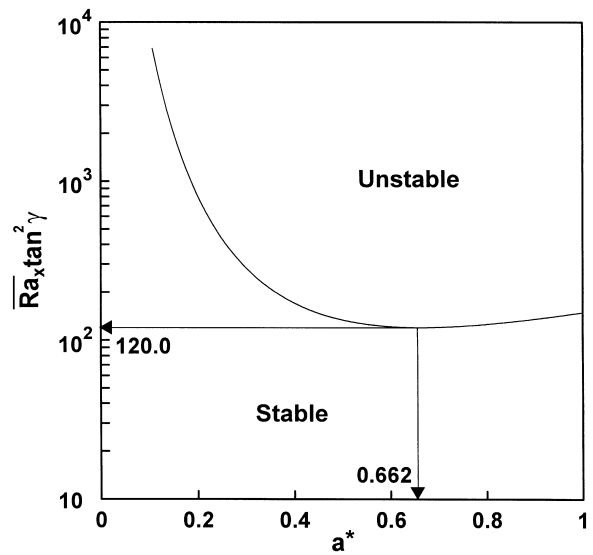


Fig. 3. Neutral stability curve for $Gr = B = 0$.

for the case of $\partial u_1 / \partial x = 0$ is nearly equal to that of $\partial u_1 / \partial x \neq 0$ when \bar{Gr} is small. As \bar{Gr} increases, the difference becomes larger and therefore, $\partial u_1 / \partial x$ cannot be neglected. Its value increases with \bar{Gr} , i.e. inertia effects make the system more stable. This trend is different from the result by Chang and Jang [13]. Their result for a horizontal case shows that inertia effects make the system more unstable. But, they used Forchheimer's model improperly. Forchheimer's model has the inertia term, $b|\mathbf{u}|\mathbf{u}$. By the linear stability analysis, substituting Eq. (14) into the governing equations, the inertia terms are obtained as $b|\mathbf{u}_0 + \mathbf{u}_1|(\mathbf{u}_0 + \mathbf{u}_1)$

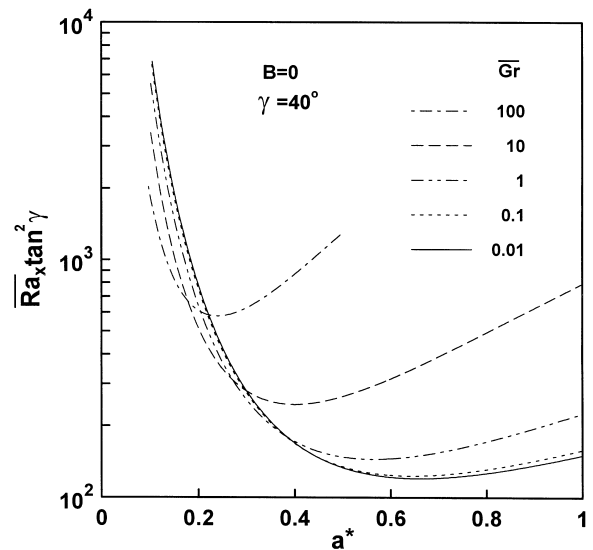


Fig. 4. Neutral stability curves for various \bar{Gr} -values.

Table 2
Predicted values of $\overline{Ra}_{x,c} \tan^2 \gamma$ and a_c^* for $B = 0$

\overline{Gr}	γ (°)	a_c^*	$\overline{Ra}_{x,c} \tan^2 \gamma$
0.01	20–60	0.66	120.3
0.1	20–60	0.643	123.2
1	20–40	0.563	144.9
	50	0.563	145.1
10	60	0.563	145.4
	20–30	0.399	245.4
	40	0.399	245.7
100	50	0.399	246.0
	60	0.4	246.9
	20–30	0.24	578.1
	40	0.24	578.6
	50	0.24	580.0
	60	0.241	583.5

$|\mathbf{u}_0 + \mathbf{u}_1| \approx |\mathbf{u}_0|$ since disturbed quantities are infinitesimal. Thus, by subtracting the parts satisfied by the basic quantities the inertia terms are obtained as $b|\mathbf{u}_0\mathbf{u}_1$. This is shown clearly in Eqs. (17)–(19). But Chang and Jang [13] used bw_0w_1 in the z -momentum equation and neglected the inertia term in the y -momentum equation. Because of their improper treatment of the inertia effects, their results are contrary to ours.

The stability conditions under no dispersion effect are listed for various γ -values in Table 2 for $20^\circ \leq \gamma \leq 60^\circ$. In this γ -range the $\overline{Ra}_{x,c} \tan^2 \gamma$ value is almost the same for a given \overline{Gr} . Based on Table 2, the stability criteria for $B = 0$ can be well represented with an error bound of 5% by the following correlations, as shown in Fig. 5:

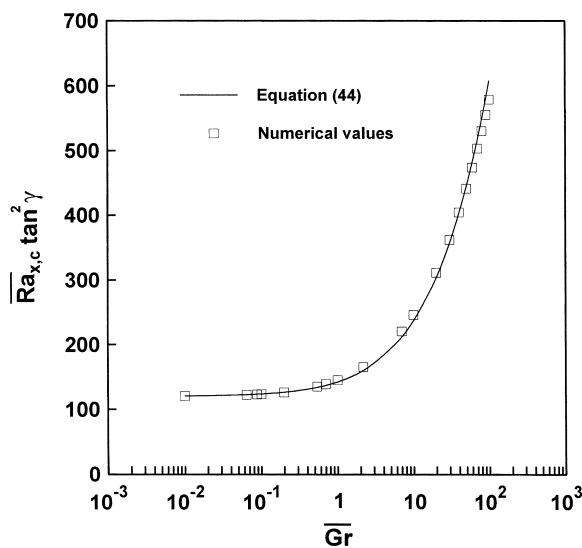


Fig. 5. Effects of \overline{Gr} on stability condition for $B = 0$.

$$\overline{Ra}_{x,c} \tan^2 \gamma \cong 120(1 + 0.311\overline{Gr}^{0.8})^{0.625} \tag{44a}$$

$$\tilde{x}_c = \frac{x_c}{L} \cong \frac{120(1 + 0.311(Gr \cos \gamma)^{0.8})^{0.625}}{(Ra_L \sin \gamma \tan \gamma)} \tag{44b}$$

Eq. (44b) is a transformation of Eq. (44a). The critical position \tilde{x}_c to mark the onset of longitudinal vortex rolls becomes smaller with an increase in Ra_L and γ and with a decrease in \overline{Gr} . It is stressed that the present predictions cover the range of $25^\circ \leq \gamma \leq 60^\circ$, of which the reason will be discussed later in comparison with experimental results.

The thermal dispersion effects on the critical conditions for $\gamma = 40^\circ$ are shown in Fig. 6. As expected, the inertia effect of \overline{Gr} makes the system stable. $\overline{Ra}_{x,c} \tan^2 \gamma$ experiences the minimum for $\overline{Gr} \leq 1$ but for $\overline{Gr} > 1$ it decreases monotonically as $\overline{B}Ra_d$ increases. This means that the dispersion makes the system unstable for $\overline{Gr} > 1$ but for $\overline{Gr} \leq 1$ it brings the stabilizing effect over the certain $\overline{B}Ra_d$ -value depending on \overline{Gr} . Coupled effects of both inertia and dispersion (see Eqs. (6) and (7) and also Fig. 6) seem to be bringing this peculiar behavior.

The effect of the inclination angle γ on $Ra_{x,c}$ for $\overline{B}Ra_d = 1$ is shown in Fig. 7. As γ increases, the system becomes more unstable. The infinite value of $Ra_{x,c}$ at $\gamma = 0^\circ$ implies that the vortex mode of instability will not manifest itself in natural convection flow over a vertical surface. In other words, the larger the inclination angle with respect to the vertical, the more susceptible the steady longitudinal vortex mode of disturbances is. In the limit of $\gamma = 0^\circ$ the flow is stable for this form of disturbances. For small inclination

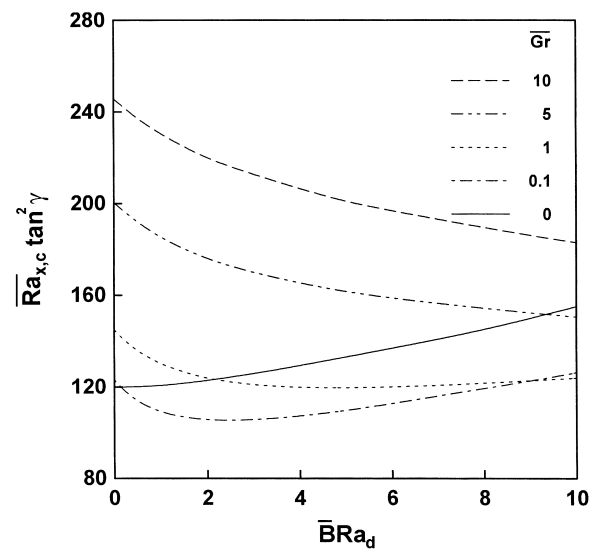


Fig. 6. Dispersion effects on stability condition for $\gamma = 40^\circ$.

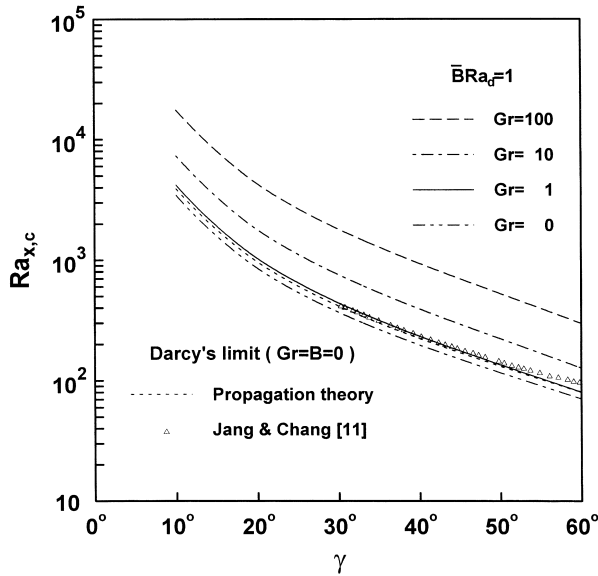


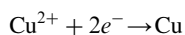
Fig. 7. Effect of inclination angle γ on $Ra_{x,c}$ for $\bar{B}Ra_d = 1$.

angles the instability will be characterized by the T–S (Tollmien–Schlichting) wave instability. The present predictions for $Gr = B = 0$ are also compared with those of Jang and Chang [11] in Fig. 7. For small γ , their results show good agreement with the present ones but for large γ their predictions are slightly higher. This difference comes from the analysis for the undisturbed flow. Their analysis does not admit similarity solutions for the basic flow and neglects the term $\partial u_1 / \partial x$ in the continuity equation for the disturbed state. To support the present predictions the ionic mass transfer experiments were conducted.

3. Experiments

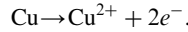
3.1. Electroplating experiments

The system of buoyancy-driven convection used in the present experiments is that of the electrochemical redox reaction of copper ion in aqueous copper sulfate solution. This system has been widely used in studying buoyancy-driven phenomena because copper sulfate has a reasonable solubility in water at room temperature. It is chemically stable and does not form soluble product on the electrode surface. In the present experiments copper plates were used as both the cathode and the anode. At the cathode the following reduction reaction occurs:



while the following oxidation reaction proceeds at the

anode:



Sulfuric acid was added as a supporting electrolyte to lessen the electromigration effect. Copper was deposited on the cathode electrode and it was dissolved from the anode one. The cathode reaction is intrinsically a surface reaction and it causes change in the electrolyte composition near the surface. A thin layer, impoverished in copper ions, develops at the cathode surface and natural convection flow occurs as a density gradient develops over the bottom cathode on passing current.

The experimental apparatus is schematized in Fig. 8. The plastic bath was filled with glass balls of 5.1 or 3 mm diameter. The vertical anodic copper plate was 8 cm wide and 9 cm long. The inclined cathodic copper plate was 5 cm wide and the distance between the electrodes was 10 cm. The backside of each electrode was stuck on the plastic plate. The glass balls were saturated with the electrolyte that consisted of 0.1 M $CuSO_4$ solution with 1.5 M H_2SO_4 as a supporting electrolyte. The calomel reference electrode was used to measure the potential difference between the electrolyte solution and the cathode. The limiting current densities were measured by a potentiostat (EG&G PARC, model M263A). Experiments were repeated at room temperature under various inclination angles ($\gamma = 0-60^\circ$) and plate lengths of cathode ($L = 0.1-8$ cm). From the measured limiting current densities the critical distance x_c to mark the onset of instability was determined. x_c ranged from 2 to 8 mm, depending on γ .

3.2. Determination of physical properties

The density and viscosity of fluid were calculated by using the correlations of Fenech and Tobias [25]. The measured porosity value ϵ was 0.42 for $d_p = 5.1$ mm and 0.40 for $d_p = 3$ mm. With these values, the For-

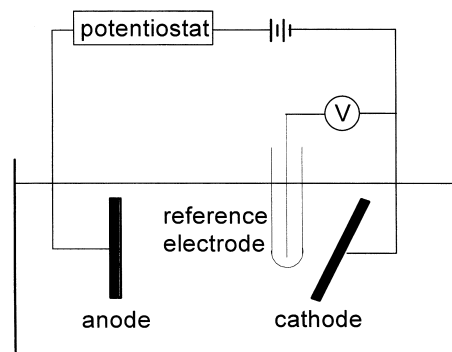


Fig. 8. Schematic diagram of present experimental system.

chheimer constant b was calculated by using Eq. (10). The permeabilities of the present porous systems were measured from the experiments using Darcy's law. For these experiments the fixed bed was built of randomly packed glass spheres placed in a cylindrical plastic container and two sensors of a manometer were positioned at the center of the cylinder. The measured permeability K was $3.812 \times 10^{-8} \text{ m}^2$ for $d_p = 5.1 \text{ mm}$ and $1.125 \times 10^{-8} \text{ m}^2$ for $d_p = 3 \text{ mm}$ from the relation of $K = \mu V d / (A \Delta p)$. μ , V , d , A and Δp denote the viscosity of water, the volumetric flow rate, the distance between two sensors of the manometer, the cross-sectional area of the plastic container and the pressure drop, respectively. These values agreed well with those from Eq. (5).

The effective molecular mass diffusivities were measured by chronoamperometry [26]. For these experiments two horizontal electrodes were used and experiments were conducted at an initially quiescent conditions (cathode facing downward). In chronoamperometry the variation of the current density with time t is measured. When the current density is plotted against $1/t^{1/2}$, the effective molecular mass diffusivity can be calculated from the slope of the straight line. The related experimental results are plotted in Fig. 9. The measured D_0 -value was $4.033 \times 10^{-6} \text{ cm}^2/\text{s}$ for $d_p = 5.1 \text{ mm}$ and $3.057 \times 10^{-6} \text{ cm}^2/\text{s}$ for $d_p = 3 \text{ mm}$. That of pure solution was $5.786 \times 10^{-6} \text{ cm}^2/\text{s}$. At 22°C , its value is $5.554 \times 10^{-6} \text{ cm}^2/\text{s}$ from the correlation of Fenech and Tobias [25]. The measured values of the effective molecular diffusivity under no motion (D_0) and the permeability (K) were used in calculating the parameters. It is very difficult to know D_0 or α_0 in

actual systems. But here the direct measurement of D_0 made it more reliable to compare predictions with experimental results.

3.3. Results and comparison

The typical limiting current density curve is shown in Fig. 10. On increasing the applied potential difference slowly, the current at first increases rapidly and then reaches a saturation level as is evidenced by a current 'plateau'. Only upon relatively higher increase of the applied potential, the current rises appreciably again. At this stage, the hydrogen ions take part in electrochemical reaction and hydrogen gas bubbles evolve. The point at which an increase in potential difference causes almost no increase in current density is known as the limiting current density. Under the limiting current condition the average mass transfer coefficient h_L equivalent to the average heat transfer coefficient over the plate length L can be obtained from the relation of

$$h_L = \frac{I_{\text{lim}}(1 - t_n)}{C_b n F} \quad (45)$$

where t_n is the transference number which explains the migration effect. I_{lim} , n , F and C_b denote the limiting current density, the valence of the transferred ion, Faraday's constant and the bulk concentration of the transferred ion, respectively. Then, the average Sherwood number Sh_L based on $(C_b - C_s)$ with the concentration at the cathode surface $C_s = 0$ can be expressed as:

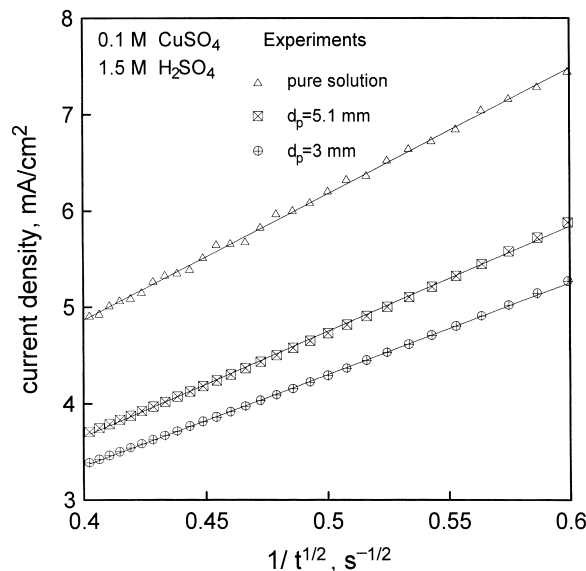


Fig. 9. Current density vs. inverse of the square root of time.

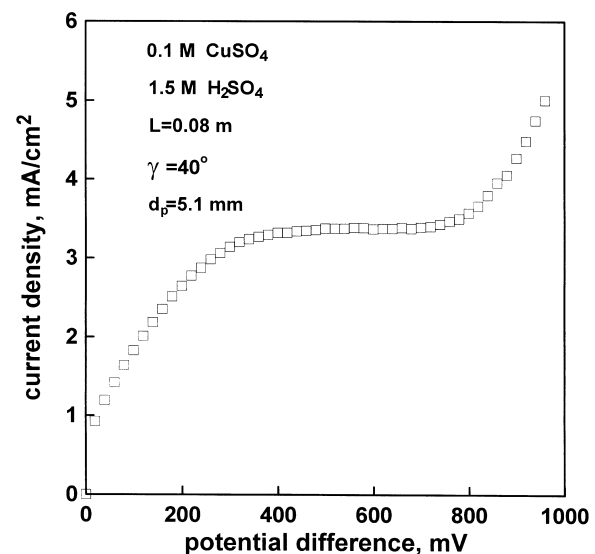


Fig. 10. Typical curve of current density vs. potential.

$$Sh_L = \frac{h_L L}{D_0} = \frac{I_{lim}(1 - t_n)L}{C_b D_0 n F} \quad (46)$$

where L is the length of the cathode electrode.

In the primary flow of stable natural convection the average Sherwood number Sh_0 can be obtained by averaging the local Nusselt number of Eq. (13) since an analogy between mass transfer and heat transfer exists:

$$Sh_0 = -2[1 + \bar{B}Ra_d f'(0)]\theta'_0(0)(Ra_L \cos \gamma)^{1/2} \quad (47)$$

where the Darcy–Rayleigh number $Ra_L [= gKL\Delta\rho/(D_0\nu\rho_b)]$ and the Grashof number $Gr [= gbK^2\Delta\rho/(\nu^2\rho_b)]$ are defined, based on the density difference $\Delta\rho [= \rho_b - \rho_s]$. ρ_b denotes the bulk density and ρ_s the surface density. With $B = 0$ the above Sh_L -value is well represented by

$$Sh_0 = 0.8876(1 + 0.73(Gr \cos \gamma)^{0.735})^{-0.34}(Ra_L \cos \gamma)^{1/2} \quad (48)$$

which constitutes the minimum bound, as shown in Fig. 11. Eq. (47) with $\bar{B} = 0.0069$ agrees well with the experimental data of the primary flow but it disagrees with data points after instability sets in. In the present mass transfer system the $\bar{B}Ra_d$ -value is 2.97 for $d_p = 5.1$ mm and 1.53 for $d_p = 3$ mm.

The thermal dispersion constant B increases with increasing inclination angle γ with a fixed \bar{B} . In this primary convection regime of experiments the boundary-layer thickness are so small because $x_c < 1$ cm. With $d_p = 3$ mm and $\gamma = 40^\circ$, the thermal boundary-layer thickness is estimated to be 2.3 mm, the hydrodynamic one to be 9.4 mm, and the critical wave

length to be 3.8 mm at $x_c \approx 5.2$ mm (see Fig. 11). Therefore, in the present experimental range \bar{B} involves both inhomogeneity and channeling effects near the wall. Because the channeling effect is not so large, Sh_0 seems to be still almost proportional to $(Ra_L \cos \gamma)^{1/2}$. Hong et al. [15] reported that the thermal enhancement due to the wall-channeling effect is largely reduced because of both wall and inertia effects. Also, Renken and Poulikakos [27] showed that in experiments of laminar forced-convection heat transfer with $d_p = 3$ mm non-Darcian effects become insignificant for $x/\sqrt{K} < 1000$ with $Re_p < 30$. Re_p denotes the Reynolds number having the length scale d_p . Based on the average velocity, it is estimated that for the present system of $d_p = 3$ mm and $\gamma = 40^\circ$, $Re_p = 12.7$ and $x/\sqrt{K} = 49$ at x_c . Therefore the basic state of present experiments may exclude variable porosity effects to a certain degree like the work of Vafai and Tien [28].

As the bottom plate length L increases, Sh_0 begins to deviate from Eq. (47). The deviation point was taken as the critical position x_c to mark the onset of the secondary flow due to the unstable condition. $Ra_{x,c}$ determined from the experiments for various inclination angles are compared with the predicted $Ra_{x,c}$ -values in Fig. 12. The former values listed in Table 3 are a little higher than predictions from Eq. (44) for $\gamma \geq 25^\circ$. Once instabilities set in, their growing distance will be required until manifest vortex flows are detected experimentally. Thus it may be stated that the present predictions constitute a minimum bound. But in the range of $\gamma \leq 20^\circ$ the measured value is smaller than the prediction and therefore, the present pre-

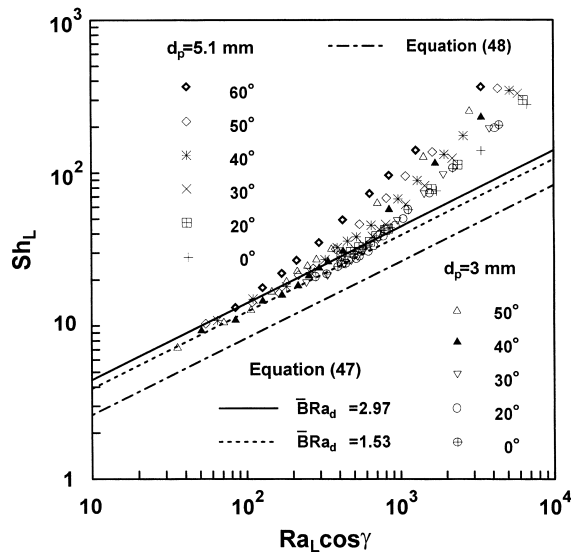


Fig. 11. Comparison of mass transfer correlation with experimental data with $\bar{B} = 0.0069$.

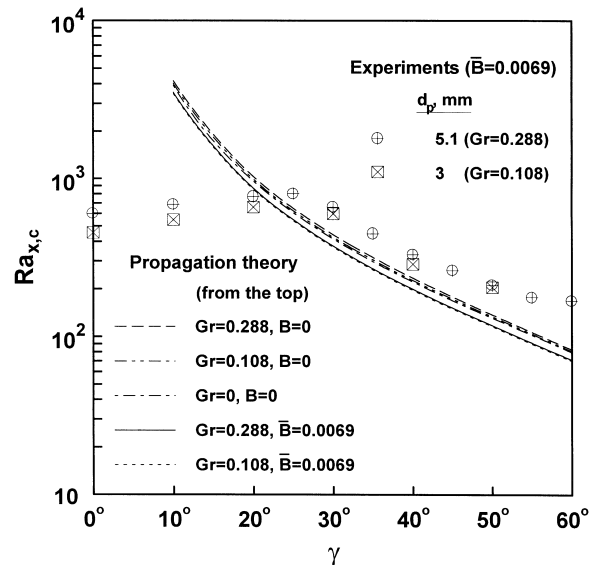


Fig. 12. Comparison of critical condition with experimental data.

dictions are useful for $\gamma \geq 25^\circ$. This is because for small γ the T–S wave instability sets in faster than the regular vortex instability. In $\gamma = 0^\circ$ the instability will be characterized by the time-dependent T–S wave only. The $Ra_{x,c}$ -values predicted from the experimental values of Gr and \bar{B} are lower than Darcian case of $Gr = B = 0$ (see Fig. 6). In the present experimental range the effects of B and Gr on x_c are not so significant, as mentioned before.

In an initially quiescent, horizontal porous layer Byun et al. [29] showed that the variable porosity and the larger particle bring destabilizing in the inhomogeneous system. As mentioned before, the inertia effect makes the system stable. The present predictions follow these behaviors for $\overline{Gr} > 1$, but under the present experimental conditions of $\overline{Gr} < 1$ and $\bar{B}Ra_d > 1.5$ it is shown that the system of a smaller diameter, i.e. a smaller $\bar{B}Ra_d$ -value, is more unstable, as illustrated in Fig. 6. Even though the difference between the present two particle-size systems is small, these trends are seen in Fig. 12. Also, it is mentioned that the present mass transfer systems are analogous to those of heat transfer for the case of zero solid conductivity.

For $30 \leq Sh_L \leq 400$ the experimental Sh_L -values were correlated with

$$\frac{Sh_L}{Sh_0} = \left[1 + \left(\frac{Sh_1}{Sh_0} \right)^n \right]^{1/n} \quad \text{for } Ra_L \geq Ra_{x,c} \quad (49a)$$

$$Sh_1 = A(Ra_L - Ra_{x,c}) \quad (49b)$$

where Sh_1 represents thermal enhancement by the secondary flow. The exponent having the integer n was tested with $n = 1-6$. The experimental data points were well fitted with $n = 2$ for $0^\circ \leq \gamma \leq 20^\circ$ and with $n = 3$ for $30^\circ \leq \gamma \leq 60^\circ$. This difference between these two n -values may be caused by the different secondary flow behavior, i.e. T–S wave vs. longitudinal vortex flow. The A -values fitted to the experimental data of $Sh_L \geq 100$ are listed in Table 3. The A -value increases

Table 3
Experimental $Ra_{x,c}$ and A fitted to each set of data points for a given γ in Eq. (49)

d_p	5.1 mm		3 mm	
	$Ra_{x,c}$	A	$Ra_{x,c}$	A
γ ($^\circ$)				
0	601	0.0392	455	0.0454
20	770	0.0438	660	0.0440
30	660	0.0520	599	0.0481
40	330	0.0542	288	0.0544
50	212	0.0550	205	0.0585
60	169	0.0560	–	–

slightly with increasing γ . For this purpose the $Ra_{x,c}$ -value in Eq. (49b) was obtained from Eq. (44) for $\gamma \geq 30^\circ$ and for $\gamma \leq 20^\circ$ it was estimated by dividing the experimental value by 1.78. This factor is the averaged ratio of the measured to the predicted $Ra_{x,c}$, as is seen in Fig. 12. With these A -values, Sh_L represents the experimental results well.

With the A -value averaged for $\gamma \leq 20^\circ$ Eq. (49) of $n = 2$ is compared with the experimental data in Fig. 13. It is supposed that for $Ra_L > 1000$ turbulent flow exists due to the T–S waves. For $\gamma \geq 30^\circ$ the average A -value is a little higher than that of $\gamma \leq 20^\circ$. This represents that the longitudinal vortex roll enhances the heat transfer more than the T–S wave does. In Fig. 14 Eq. (49) of $n = 3$ is compared with the experimental data of $30^\circ \leq \gamma \leq 60^\circ$ for $d_p = 5.1$ mm. With $A = 0.0540$, the agreement looks good and that of $d_p = 3$ mm also agrees well (compare A -values in Table 3). With longitudinal vortex rolls of $1000 < Ra_L < 7000$ the flow seems to be almost laminar because $Re_p = O(10)$ in the present experiments. Seguire et al. [30] reported that in forced convection the turbulent region exists for $Re_p > 180$.

For $0^\circ \leq \gamma \leq 60^\circ$, the d_p -effect seems significant and Sh_L/Sh_0 of $d_p = 3$ mm is higher than that of $d_p = 5.1$ mm for $Ra_L \geq 1000$. This may mean that $\bar{B}Ra_d$ -effect in Eq. (47), i.e. the transverse thermal dispersion is still dominant like the primary laminar flow, as shown in Fig. 11. With the secondary longitudinal vortex flow, the effect of primary flow on Sh_L will be weakened (see Eq. (49a)) and the thermal dispersion will become 3D. Therefore the γ -effect on Sh_L may become insignificant in fully-developed state of extremely large Ra_L

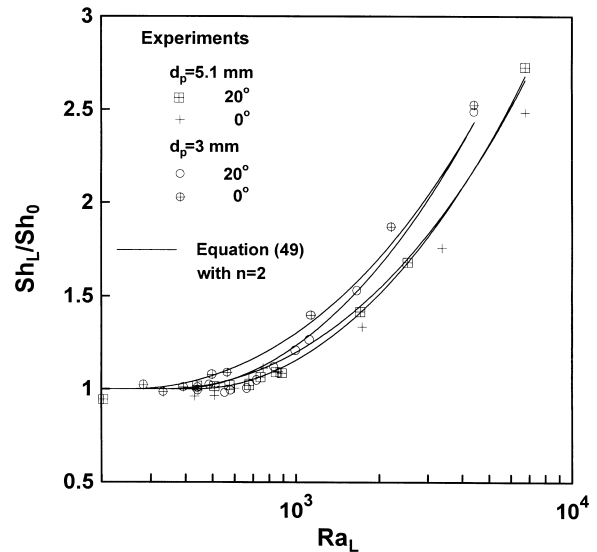


Fig. 13. Sherwood number vs. Darcy–Rayleigh number with $A = 0.0431$ for $\gamma = 0^\circ$ and 20° .

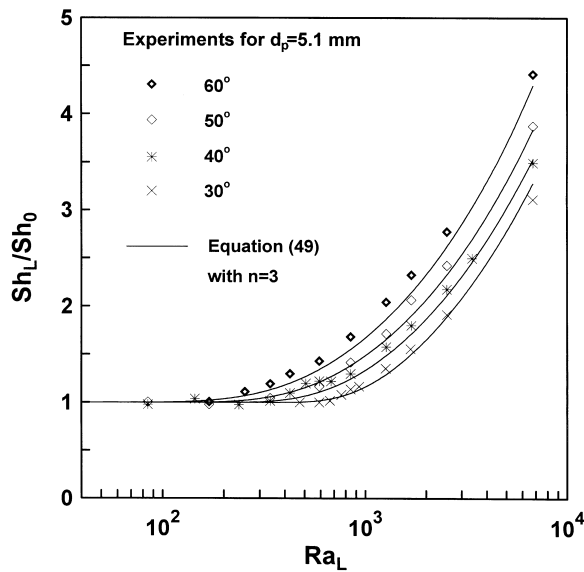


Fig. 14. Sherwood number vs. Darcy-Rayleigh number with $A = 0.0540$ for $30^\circ \leq \gamma \leq 60^\circ$.

and Eq. (49b) may be possible. Even in the case of simple horizontal porous layers, Yoon and Choi [31] showed that the Nu_L -correlation depends strongly on bK/L in addition to Ra_L and Gr . With increasing Ra_L the transport mechanism becomes very much complicated. In this connection more refined experiments and theory are required. It is stressed that Eq. (49) should be used for $Sh_L \leq 400$.

4. Conclusions

The condition of the onset of regular longitudinal vortex rolls in natural convection flow over an inclined impermeable surface in a porous medium was analyzed theoretically and experimentally. For $25^\circ \leq \gamma \leq 60^\circ$ the stability analysis involving inertia and dispersion effects was conducted by modifying Forchheimer's model under the propagation theory which we have developed. The inertia effect makes the system more stable and for $\overline{Gr} > 1$ the thermal dispersion effect more unstable. But for $\overline{Gr} < 1$ the dispersion effect makes the system either more stable or more unstable depending on the $\overline{BRa_d}$ -value. With increasing γ the system becomes more unstable. To support the present predictions, experiments of electrochemical ionic mass transfer were conducted for $50 \leq Ra_L \leq 7000$ and $7 \leq Sh_L \leq 400$. Predictions resulting from the measured permeability and mass diffusivity represented experimental data reasonably well for $\gamma \geq 20^\circ$. For $0 \leq \gamma \leq 60^\circ$ new Sh_L -correlations were proposed as a function of Sh_0 , $Ra_{x,c}$ and Ra_L .

Acknowledgements

This work was supported under research grants by the Alumni Association of Department of Chemical Engineering, Seoul National University.

References

- [1] H. Benard, Les tourbillons cellulaires dan une nappe liquide transportant de la chaleur par convection en regime permanent, *Annales de Chimie el de Physique* 23 (1901) 62–144.
- [2] Lord Rayleigh, On convection currents in a horizontal layer of fluid when the higher temperature is on the under side, *Philosophical Magazine* 32 (1916) 529–543.
- [3] E.M. Sparrow, R.B. Husar, Longitudinal vortices in natural convection flow on inclined plates, *J. Fluid Mech* 37 (1969) 251–255.
- [4] J.R. Lloyd, E.M. Sparrow, On the instability of natural convection flow on inclined plates, *J. Fluid Mech* 42 (1970) 465–470.
- [5] G.J. Hwang, K.C. Cheng, Thermal instability of laminar natural convection flow on inclined isothermal plates, *Canadian J. Chem. Eng* 51 (1973) 659–666.
- [6] S.E. Haaland, E.M. Sparrow, Vortex instability of natural convection flow on inclined surfaces, *Int. J. Heat Mass Transfer* 16 (1973) 2355–2367.
- [7] T.S. Chen, K.L. Tzuoo, Vortex instability of free convection flow over horizontal and inclined surfaces, *J. Heat Transfer* 104 (1982) 637–643.
- [8] I.G. Hwang, M.Y. Hong, C.K. Choi, Vortex instability of laminar natural convection flow and heat transfer over constant-heat-flux inclined plates, in: *Proceedings of the Second European Thermal-Sciences and the Fourteenth UIT National Heat Transfer Conference*, Edizioni ETS, Rome, vol. 2, 1996, pp. 819–826.
- [9] P. Cheng, W.J. Minkowycz, Free convection about a vertical flat plate embedded in a porous medium with application to heat transfer from a dike, *J. Geophysics Res* 82 (1977) 2040–2044.
- [10] C.T. Hsu, P. Cheng, Vortex instability in buoyancy-induced flow over inclined heated surfaces in a porous media, *J. Heat Transfer* 101 (1979) 660–665.
- [11] J.Y. Jang, W.J. Chang, Vortex instability of buoyancy-induced inclined boundary layer flow in a saturated porous medium, *Int. J. Heat Mass Transfer* 31 (1988) 759–767.
- [12] O.A. Plumb, I.C. Huenefeld, Non-Darcy natural convection from heated surfaces in saturated porous media, *Int. J. Heat Mass Transfer* 24 (1981) 765–768.
- [13] W.J. Chang, J.Y. Jang, Inertia effects on vortex instability of a horizontal natural convection flow in a saturated porous medium, *Int. J. Heat Mass Transfer* 32 (1989) 541–550.
- [14] O.A. Plumb, The effect of thermal dispersion of heat transfer in packed bed boundary layers, *Proceedings of ASME-JSME Thermal Engineering Joint Conference 2* (1983) 17–22.
- [15] J.T. Hong, Y. Yamada, C.L. Tien, Effects of non-

- Darcian and nonuniform porosity on vertical-plate natural convection in porous media, *J. Heat Transfer* 109 (1987) 356–362.
- [16] I.G. Hwang, C.K. Choi, An analysis of the onset of compositional convection in a binary melt solidified from below, *J. Crystal Growth* 162 (1996) 182–189.
- [17] K.H. Kang, C.K. Choi, A theoretical analysis of the onset of surface-tension-driven convection in a horizontal liquid layer cooled suddenly from below, *Physics of Fluids* 9 (1997) 7–15.
- [18] M.C. Kim, J.S. Baik, I.G. Hwang, D.Y. Yoon, C.K. Choi, Buoyancy-driven convection in plane Poiseuille flow, *Chem. Eng. Sci* 54 (1999) 619–632.
- [19] M.C. Kim, K.H. Choi, C.K. Choi, The onset of thermal convection in an initially, stably stratified fluid layer, *Int. J. Heat Mass Transfer* 42 (1999) 4253–4258.
- [20] K. Chen, M.M. Chen, Thermal instability of forced convection boundary layers, *J. Heat Transfer* 106 (1984) 284–289.
- [21] K. Chen, Thermal instability of wedge flows, PhD thesis, University of Illinois at Urbana-Champaign, Urbana, IL, USA, 1981.
- [22] K. Chen, M.M. Chen, C.W. Sohn, Thermal instability of two-dimensional stagnation-point boundary layers, *J. Fluid Mech* 132 (1983) 49–63.
- [23] M.C. Kim, The onset of natural convection and heat transfer correlations in systems experiencing thermal boundary layer characteristics, PhD thesis, Seoul National University, Seoul, South Korea, 1992.
- [24] O.T. Hanna, O.C. Sandall, *Computational Methods in Chemical Engineering*, Prentice-Hall, New Jersey, 1995.
- [25] E.J. Fenech, C.W. Tobias, Mass transfer by free convection at horizontal electrodes, *Electrochemical Acta* 2 (1960) 311–325.
- [26] E. Heitz, G. Kreysa, in: *Principles of Electrochemical Engineering*, VCH Publishers, New York, 1986, pp. 14–15.
- [27] K.J. Renken, D. Poulikakos, Experiments on forced convection from a horizontal heated plate in a packed bed of glass spheres, *J. Heat Transfer* 111 (1989) 59–65.
- [28] K. Vafai, C.L. Tien, Boundary and inertia effects on flow and heat transfer in porous media, *Int. J. Heat Mass Transfer* 24 (1981) 195–203.
- [29] S.H. Byun, I.G. Hwang, C.K. Choi, Thermal instabilities in horizontally superposed fluid and porous layers with variable porosity, *Hwahak Konghak* 35 (1997) 921–927.
- [30] D. Seguin, A. Montillet, J. Comiti, Experimental characterisation of flow regimes in various porous media—I: limit of laminar flow regime, *Chem. Eng. Sci* 53 (1998) 3751–3761.
- [31] D.Y. Yoon, C.K. Choi, Thermal convection in a saturated porous medium subjected to isothermal heating, *Korean J. Chem. Eng* 6 (1989) 144–149.